Fig. 1. Schematic diagrams of the generation process and cardiomyocyte monitoring of the anisotropic Janus SCPs. (**A**) Generation process of the anisotropic Janus SCPs. (**B**) Preparation process of the anisotropic hydrogel SCPs. (**C**) Construction of cardiomyocyte monitoring platform by the anisotropic hydrogel SCPs.
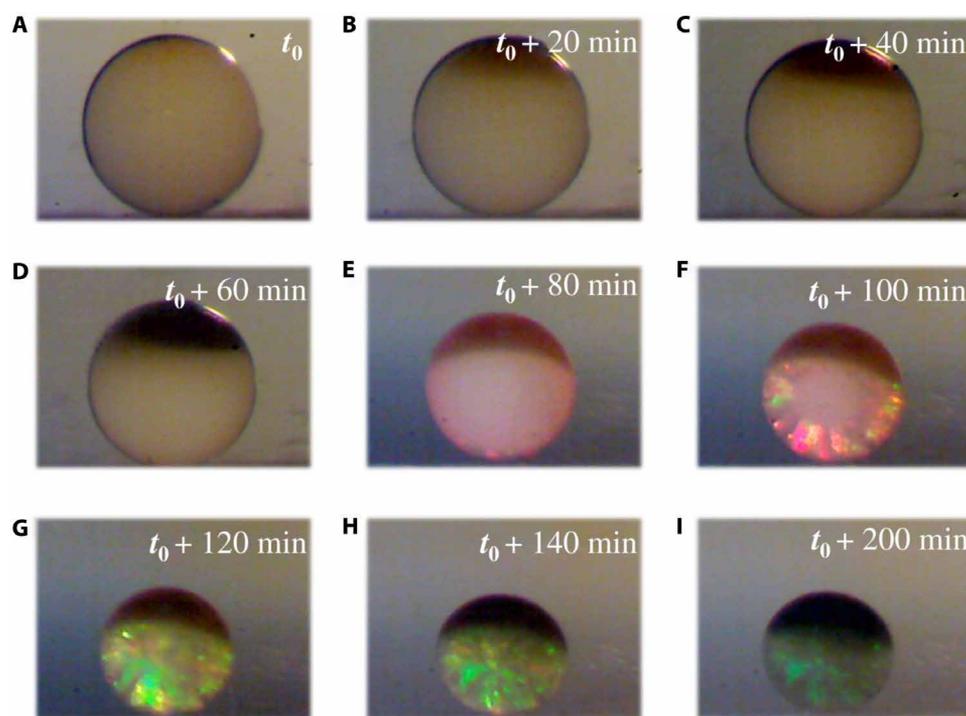
Fig. 2. The phase separation phenomenon of GO and silica nanoparticles in a droplet during the heating process. (**A** to **I**) The optical images of a droplet at different time during the heating process.

droplet templates demonstrated phase separation behavior and Janus structure beyond expectation. This phenomenon could be ascribed to the following three reasons: ions (pH), density, and assembly time. First, the ions of the GO solution affected the stability of the silica nanoparticles in water. As the silica nanoparticles used in this study were prepared by the hydrolysis of tetraethoxysilane, there were many Si-OH groups on the surface of the nanoparticles that could ionize in the solution; hence, the nanoparticles exhibited neg-

ative charge and were mutually exclusive, and their total interparticle potential in the solution was comparatively balanced. On the contrary, when some ions or acids were added into the solution, the absolute value of the zeta potential of the nanoparticles would notably reduce, which meant the repulsion among the nanoparticles was weakened and the balance was broken, so that the nanoparticles tended to deposit (35–37). Therefore, the addition of the GO (pH 1.88) would suppress the ionization of the silica nanoparticles, which

resulted in a reduced charge and lower repulsive force of the nanoparticles and, thus, caused the break of the stable state and the deposition of the nanoparticles (fig. S1 and table S1). As the diameters of the nanoparticles in the mixed solution calculated by the Stokes' law (360 nm) and measured by the granulometer (about 298 nm) were all close to the original value before mixing with GO [about 250 nm from scanning electron microscope and 287 nm from granulometer], there was little aggregation in the mixed solution (the specific calculation process of the size of the nanoparticles through the Stokes' law is presented in the Supplementary Materials). We also prepared and observed the colloidal array formed at the similar pH condition without GO by adding acid solution. It was found that the assembled particles could form a uniform spherical structure, but the arrangement of the nanoparticles observed by scanning electron microscopy (SEM) was disordered (fig. S2, A and B). This result might be ascribed to the introduced acid radical ions in the pH tuning process. To confirm this deduction, we assembled sulfonic-group–modified nanoparticles in droplets (pH 1.74) to avoid the interference of other ions and observed their resultant microstructures by SEM. It was observed that the surface and interior of the assembled particles were all with ordered hexagonal-close-packed (HCP) microstructures (fig. S2, C and D). Next, the silica nanoparticles had greater densities than the GO; its layer would settle at the bottom of the resultant Janus particles. As a result, the low-density GO would concentrate in the upside and thereby form a two-layer structure. The last reason is that the phase separation process is relatively time-consuming; many methods like spray coating can be completed in a short time, and therefore, the Janus structure could not be finished and observed through these protocols.

The crystallization of the colloidal array was attributed to the solvent evaporation. In this case, the loss of solvent would squeeze the silica nanoparticles in the droplets, and then the nanoparticles would self-assemble into an HCP structure according to the lowest energy principle. The GO could be reduced at 70°C depending on the addition of a reducing agent. However, in our study, we did not used a reducing agent with GO, so the GO could not be reduced during the drying process. During the droplet shrinkage, the GO would aggregate and eventually dry together because of the solvent evaporation. Thus, after the solvent totally evaporated, the Janus particles with the GO-enriched top section and the silica nanoparticle crystalline bottom section could be obtained. Then, these Janus particles were then calcined under the protection of argon to acquire a higher mechanical strength, and the GO was lastly transformed into reduced GO (rGO) with darker colors. The microstructure of the resultant anisotropic SCPs was characterized by SEM. As shown in Fig. 3A, the anisotropic SCP was composed of a hemispherical section and an oblate part. With higher magnification, the silica nanoparticles self-assembled into an ordered HCP structure, which could be observed on the surface and the interior of the hemisphere (Fig. 3, B and C). The oblate part of the anisotropic SCP was also observed in detail, as demonstrated in Fig. 3D and fig. S2 (E and F); it was apparent that there was abundant GO that enriched and disordered the arrangement of silica nanoparticles in the oblate part. It is worth mentioning that there were some GO sheets that existed in the interstitial voids of the colloidal array. Actually, in most areas of the silica nanoparticle layer that is not in contact with the GO layer, the nanoparticles were not affected by the GO and thus could self-assemble into an HCP structure. However, these nanoparticles, which were close to the interface between the two layers, showed a relatively disordered micro-

structure because of the incomplete separation of the mixture at the unsmooth interface (fig. S3, A to C).

Attributed to the unique Janus microstructure, the anisotropic SCPs were endowed with distinct optical characteristics. The ordered HCP structure of the hemispheres resulted in PBGs, by which the light that matched the frequency was prohibited from spreading and reflected totally; thus, the photonic section showed vivid structural color. Under normal incidence, the reflection peak position λ of the photonic section could be estimated by the Bragg-Snell Law

$$\lambda = 1.633 d \, n_{average} \qquad (1)$$

where d is the center-to-center distance of two neighboring nanoparticles and $n_{average}$ is the average refractive index. In general, the $n_{average}$ of the photonic section composed of the same components is constant; hence, the colors of the anisotropic SCPs could be tailored by changing the diameters of the self-assembling nanoparticles, as shown in Fig. 4 (A to C and F). Meanwhile, because of the disordering and the broadband light absorption of the GO, the dark section showed a black view, which definitely helped to improve the color contrast and saturation of the photonic section and reduce the full width at half maximum (FWHM) so that the clearer structural color could be observed in this section (Fig. 4, D and E).

As the droplet templates were generated from a single emulsion microfluidic device, the size of the particles could be regulated precisely. In general, the faster outer flow rate or slower inner flow rate would result in smaller anisotropic SCPs (fig. S4). The effects of different amounts of mixed GO were also discussed. As illustrated in fig. S5, the diameter of the particles would enlarge with the increasing GO amount when the concentration of GO in the mixture was less than 3 mg/ml, while the particle size would remain invariable if the GO concentration was higher than that threshold. Besides, the mixed GO could regulate the morphology of the anisotropic SCPs. In general, the water droplets in silicon oil are kept spherical because of the surface tension. Thus, the silica nanoparticle–dispersed droplets without GO were kept spherical during the drying process (fig. S2A). In comparison, the silica nanoparticle–dispersed droplets with GO additives were separated into two layers in the silicon oil, and both the two layers tended to form the hemispherical shape. When the GO was with high concentration, the GO layer formed the hemispherical shape. However, if the GO could not reach that high concentration, then the resulting GO layer would have a small volume and thus will be thinner than the nanoparticle layer because the interface between the two layers is consistent. Therefore, the GO layer had a larger radius of curvature than the nanoparticle layer and showed a flat shape (fig. S6). For better description, we defined the thickness of the dark section as the minor axis and the diameter of the particle as the major axis (fig. S3A). Different from the major axis, the length of the minor axis was closely related to the GO concentration notably during the whole concentration range, and hence, the ratio of the minor axis to the major axis increased along with the increase in concentration of GO (fig. S3D). Moreover, it is worth noting that although the GO affected the self-assembling of silica nanoparticles in the dark section, it had little influence on the silica nanoparticles in photonic section even with high concentration (fig. S6). Thus, the reflective spectra of the anisotropic SCPs with different concentrations of GO had the same peak positions, while the intensity would reduce slightly along with the increase in
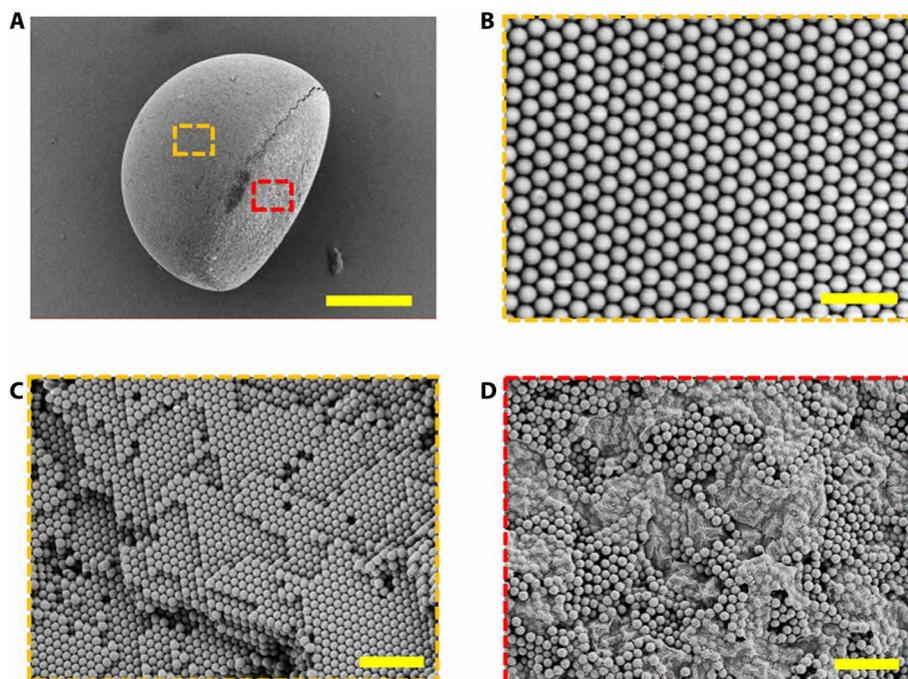
Fig. 3. The SEM images of an anisotropic SCP. (**A**) Whole view of the anisotropic Janus SCP. (**B** and **C**) Surface and inner microstructures of the photonic section framed by the yellow dash line in (A). (**D**) Surface microstructure of the dark section framed by the red dash line in (A). Scale bars, 100 μm (A), 1 μm (B), and 2 μm (C and D).
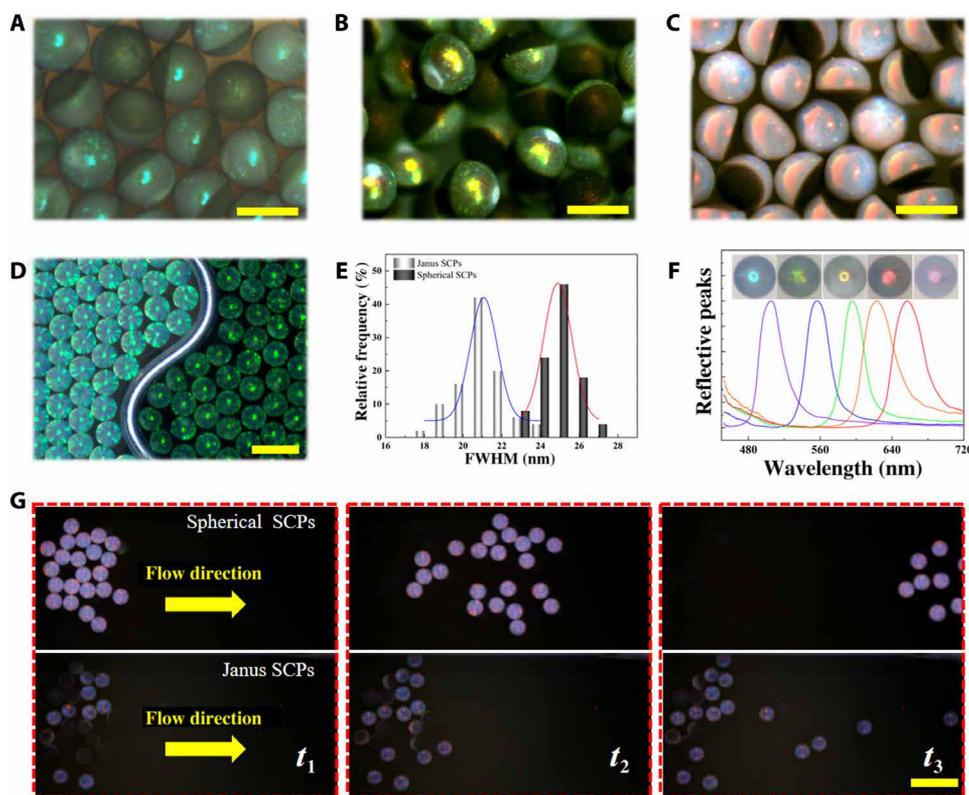
Fig. 4. The optic and morphology characterization of the Janus SCPs. (**A** to **C**) Reflection microscope images of three kinds of anisotropic Janus SCPs. (**D**) Reflection optical images of common spherical SCPs (left) and Janus SCPs (right). (**E**) FWHM distributions of the SCPs shown in (D). (**F**) Normalized reflective peaks and reflection images of five different anisotropic Janus SCPs. (**G**) Comparison of movability of spherical SCPs and anisotropic Janus SCPs in the same microfluidic channel with flow. Scale bars, 300 μm (A to C), 500 μm (D), and 1 mm (G).

GO because of the smaller photonic section and the enhanced light absorption (fig. S7A). In addition, on account of the three-dimensional hemispherical structure, the ordered photonic section of the anisotropic SCPs was endowed with an angle independence similar to the common spherical particles. It is worth noting that the Janus particles in fig. S8A exhibited a bit of red color. However, although there was little color to be observed, its reflective spectrum was much lower than of others, and thus, it seemed that the dark section had no reflective peak (fig. S7B).

The Janus structure often provides materials more functions than the homogeneous structure (38, 39). In this study, the unique Janus morphology of our designed particles not only led to a distinct optical characteristics but also imparted them the capabilities of fixation, location, and orientation. As a demonstration, the anisotropic SCPs and the spherical SCPs were put in the same kind of microfluidic channels, respectively. With a flow rate, the spherical SCPs rolled away easily. However, when the Janus SCPs suffered from fluid shock, the ones with the photonic section in contact with the channel wall would roll along with the fluid until they turned over and the dark section began to be in contact with the wall; meanwhile, the ones with the dark section in contact with the channel wall initially would only move a little distance (Fig. 4G and movies S1 and S2). These could be attributed to the specific plane structure of the oblate section, which provided higher sliding friction force and shock resistance compared with the common spherical SCPs, so that the anisotropic SCPs easily remained still on the flow. Thus, this kind of anisotropic SCPs with a previously unreported macroscopically fixable feature would have broader application prospects compared with those traditional structural color materials.

To explore the intelligent responsive capacity of the Janus particles, we used them as templates for constructing responsive structural color hydrogel particles, as illustrated in Fig. 5A. Specifically, we chose N-isopropylacrylamide (NIPAM) as monomer and N,N′-methylenebis (acrylamide) (Bis) as cross-linker in the preparation of thermal responsive particles. During the process, the pregel solution contained NIPAM, and Bis was introduced into the anisotropic SCPs and filled the voids among the nanoparticles and rGO first. After being exposed to ultraviolet (UV) light, the solution was polymerized, silica/rGO–pNIPAM [poly(NIPAM)] hybrid particles were obtained, and the porous rGO-pNIPAM anisotropic hydrogel SCPs were finally acquired after hydrofluoric acid etching. The hybrid and anisotropic hydrogel SCPs also showed vivid colors (Fig. 5B and figs. S8, A and B, and S9), which indicated that they inherited the rGO and ordered structure of the templates, and this deduction was further confirmed by the SEM images (Fig. 5, C to E, and fig. S8, C and D). On this basis, to demonstrate the dynamic regulation capability of the anisotropic hydrogel SCPs, we used a parallel near-infrared (NIR) light to trigger the particles. It has been widely confirmed that rGO has a photothermal effect because of its strong NIR absorption, and pNIPAM can reversibly shrink and swell due to the temperature change cycle. The anisotropic hydrogel SCPs combined the two features; thus, they were expected to exhibit photothermally responsive performance. As shown in Fig. 5F, figs. S10 and S11A, and movie S3, when the hydrogel particles were exposed in the NIR light, they shrank immediately and demonstrated a distinct color change. It was found that the light intensity of the NIR could also affect the degree of the volume change. The higher the light intensity was, the larger and faster the volume and reflective peaks changed (fig. S11B). These results indicated that the pNIPAM

anisotropic hydrogel SCPs have the potential to be used as photothermal switches or NIR-triggered system due to their photothermal conversion capability.

To further investigate the potential value of the anisotropic SCPs in the biomedical field, another kind of hydrogel methacrylated gelatin (GelMA) was used for constructing the hydrogel Janus SCPs. As a kind of derivation of modified extracellular matrix components, GelMA has superb biocompatibility, and thus, the GelMA anisotropic hydrogel SCPs were suitable for cell culture (fig. S12) (40–43). Similar to the pNIPAM anisotropic hydrogel SCPs, the resultant GelMA anisotropic hydrogel SCPs could also exhibit vivid colors (fig. S13, A to C). As the refractive index of GelMA is higher than that of water, the reflective peaks of the hybrid particles showed a red shift. After the silica was replaced by water, the average refractive index decreased; thus, the reflective peaks of the anisotropic hydrogel SCPs shifted notably to the blue side (fig. S13D).

Here, we used the GelMA anisotropic hydrogel SCPs as microcarriers for the culture and monitoring of the cardiomyocytes (Fig. 6A). To implement this concept, the cardiomyocytes were extracted from rats and cultured for 2 days to recover stable autonomic beating. A confocal laser scanning microscope (CLSM) was used to investigate the growth conditions of the cultured cells. As shown in Fig. 6B, the cardiomyocytes spread out on the surface of an anisotropic hydrogel SCP and showed the obvious structure of a sarcomere. This indicated that the cellular morphology of the cardiomyocytes was recovered. The cell activity was another important index to characterize the growth condition of cells. In most cases, the activities of cells were measured by methyl thiazolyl tetrazolium (MTT) or cholecystokinin octapeptide (CCK-8), which are reagent dependent, time-consuming, and multistep. Although some mechanical sensors had been studied for detecting cardiomyocyte activities, the precision-machined and complicated devices made them difficult to apply (44, 45). Here, the GelMA anisotropic hydrogel SCPs could not only culture the cardiomyocytes but also monitor the cell activities by observing the structural colors. Because the beating of the cardiomyocytes (about 20 cells) caused the shrinkage of particles during the contracting process and the return to the original shape during the relaxing process, the structural color of the photonic section would change with the cell beating process. Moreover, benefiting from the oblate built-in black background, the color change could be observed and monitored by a camera and an optic spectrometer readily and clearly (Fig. 6, C to E, and movie S4). In general, the stiffness of the hydrogel could influence the color shift induced by cells: The hydrogel with low stiffness had better responsiveness to the cells, while the highly stiff hydrogel benefited the maintenance of the inverse opal structure. Thus, the 15 weight % (wt %) GelMA was chosen as the optimized concentration for the fabrication of the Janus structure hydrogel.

As the growth condition of the cardiomyocytes could affect the frequency and strength of the beating, the fluctuation of frequency and intensity of the particle spectra could be used to monitor the cardiomyocytes activities, and thus, the particles have potentials in drug evaluation. To demonstrate their capability, we added the myocardial drug isoproterenol with different concentrations to the cell culture medium to stimulate the cardiomyocytes on the hydrogel SCPs. In general, the spectra of the hydrogel SCPs could have a shift value of about 41 nm. However, with a high concentration of isoproterenol (10^{-5} M) in the culture medium, the shift value increased to about 52 nm, and it could be found that the increase in
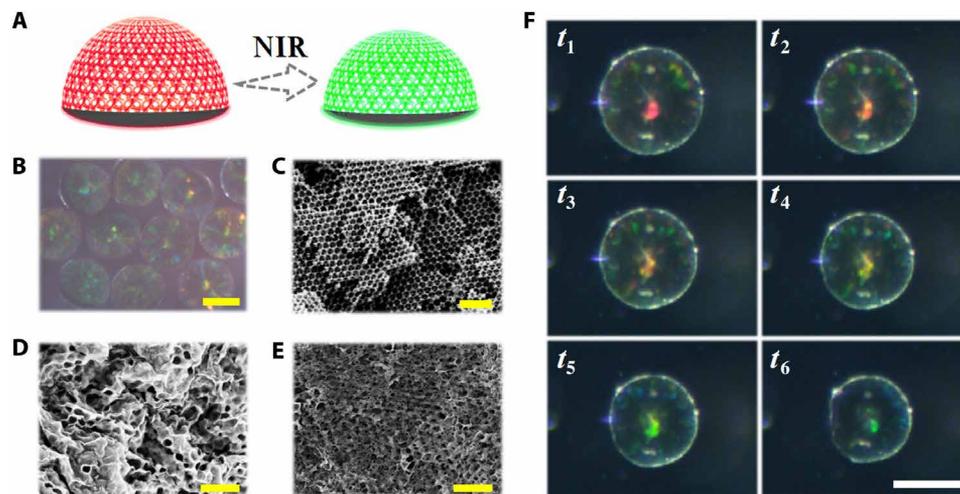
Fig. 5. The microstructures and photothermal responsiveness of NIPAM hydrogel Janus SCPs. (**A**) Schematic diagram of the responsiveness principle of photothermal responsive hydrogel Janus SCPs. (**B**) Reflection microscope images of hydrogel Janus SCPs. (**C** to **E**) SEM images of the inner microstructure of the photonic section of a hydrogel Janus SCP (C), the surface (D), and inner (E) microstructure of the dark section of a hydrogel Janus SCP. (**F**) Optical microscope images of the structural color variation process of a hydrogel Janus SCP during half photothermal response cycles (from t_1 to t_6). Scale bars, 200 μm (B and F) and 1 μm (C to E).
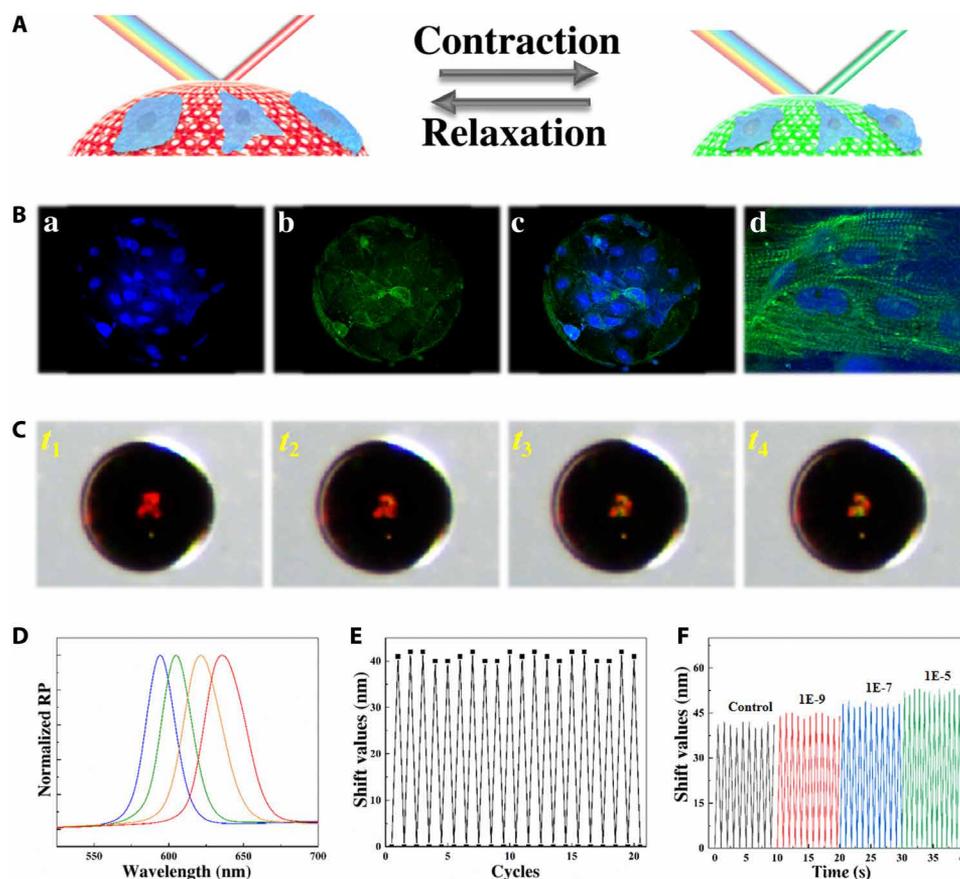
Fig. 6. The GelMA hydrogel Janus SCPs for cell culture and monitoring. (**A**) Schematic diagram of the construction of the visualized monitoring platform for cardiomyocytes on the hydrogel Janus SCPs. (**B**) Fluorescence images of the cardiomyocytes cultured on a hydrogel Janus SCP for (a) nuclei, (b) F-actin, (c) the merged field, and (d) the enlarged view of cells, respectively. (**C**) Optical microscope images of the structural color variation process of a hydrogel Janus SCP during half myocardial cycles (from t_1 to t_4). (**D**) Reflection spectra of the hydrogel Janus SCP in (C): The leftmost (blue) line corresponds to t_4 and the rightmost (red) line corresponds to t_1. (**E**) Relationship between the reflection shift values of the hydrogel Janus SCP and 20 beating cycles of the cardiomyocytes on the surface. (**F**) Relationship between the beating speed and the reflection peak shift values of the hydrogel Janus SCP treated with different concentrations of isoproterenol.

shift value was closely related to the concentration of the isoproterenol; the higher the concentration of isoproterenol the cell medium had, the larger the shift value was (Fig. 6F and fig. S14A). Besides, the isoproterenol also could regulate the beat frequency of the cardiomyocytes, which exhibited a positive chronotropic response to the concentration of the isoproterenol as well as the shift value did (Fig. 6F and fig. S14B). These results were the same as the biological effect of isoproterenol in vivo, showing increased beat intensity and frequency. Thus, the real-time spectra detection of the GelMA anisotropic hydrogel SCPs is a promising method for cell sensing, monitoring, and drug evaluation.

DISCUSSION

In summary, we presented a kind of previously unknown anisotropic SCPs by colloidal phase separation of GO and silica nanoparticles in droplets. By adjusting the different parameters in the preparation process, the anisotropic Janus SCPs with the hemispherical colloidal crystal cluster and the oblate GO component could be obtained. It was demonstrated that the designed anisotropic SCPs exhibited brilliant structural colors and the special capabilities of fixation, location, and orientation. More attractively, the derived inverse opal particles of the anisotropic SCPs not only remained the inherent vivid structural colors but were also able to be further used as intelligent responsive materials or excellent microcarriers for three-dimensional cell culture and monitoring. These results all represented the great potentials of the designed particles. Besides, through the further improvement of fabrication process and materials, we believe that the SCPs can achieve more diversified applications in more fields, such as encoding, detection, and catalysis.

MATERIALS AND METHODS
Materials
Gelatin (from porcine skin), methacrylic anhydride, pancreatin (from porcine pancreas), trypsin, 2-hydroxy-2-methylpropiophenone (HMPP), Bis, NIPAM, and octadecyltrichlorosilane were obtained from Sigma-Aldrich (St. Louis, MO, USA). Hydrofluoric acid (HF) was purchased from Aladdin Industrial Co. Ltd. (Shanghai, China). Arginine, n-hexane, ammonium hydroxide, tetraethoxysilane, sodium hydroxide, and ethanol were purchased from Sinopharm Chemical Reagent (Shanghai, China). Hanks' balanced salt solution (HBSS; 1X), fetal bovine serum (FBS), Dulbecco's modified Eagle medium/Nutrient Mixture F-12 (DMEM/F-12), 5-bromo-2-deoxyuridine (BrdU), Alexa Fluor 488 phalloidin, and 4′,6-diamidino-2-phenylindole (DAPI) were purchased from Life Technologies (USA). Collagenase type 2 was purchased from Worthington. GO solution was purchased from Nanjing XFNANO Materials Tech Co. Ltd. Cellulose dialysis membranes (molecular weight cutoff, 8000 to 14,000) were acquired from Shanghai Yuanye Biotechnology Corporation (Shanghai, China). Penicillin-streptomycin, phosphate-buffered saline (PBS), and isoproterenol were obtained from Gibco (USA). Dimethyl silicone oil with different viscosities and glassware were purchased from Nanjing Wanqing Co. Ltd. SiO_2 nanoparticles in different sizes and GelMA were self-prepared. Other reagents were analytical grade or higher, and all the reagents were used as received. Water used in all experiments was purified using a Milli-Q Plus 185 water purification system (Millipore, Bedford, MA) with resistivity higher than 18 megohm·cm.

Fabrication of GO/silica Janus particles
The GO/silica Janus particles were generated by the droplet template method. The silica nanoparticles with certain size were mixed with GO as presolution first. Then, the presolution was injected into the inner channel of a microfluidic chip, while the silicon oil was injected into the outer channel so that the presolution could be sheared into droplets by the silicon oil continuously. The concentration of the nanoparticles was adjusted to 20 wt % before used, and several GO concentrations were set as gradient. The flow rate of the silicon oil was 3 ml/hour, while the rate of presolution was 0.5 ml/hour. The resultant droplets were collected by a box with silicon oil and treated at 75°C overnight for the phase separation and the self-assembly of GO and silica nanoparticles. Then, the dried Janus particles were gently washed by n-hexane and calcined at 800°C for 4 hours with argon to enhance their mechanical strength and reduce the GO to rGO. The reflective spectra of the Janus particles were measured by a metalloscope (Guangzhou Mshot Photoelectric Technology Co., Ltd.) with a fiber optic spectrometer (Ocean Optics, USB2000+). The optical photographs of the particles were taken by a stereomicroscope (Nanjing Jiangnan Novel Optics Co. Ltd.) with a charge-coupled device camera (Media Cybernetics EvolutionMP 5.0). The microstructures of the particles were characterized by a scanning electron microscope (Hitachi, S-300 N).

Fabrication of inverse opal NIPAM hydrogel particles
Several concentrations of NIPAM pregel were prepared at first (NIPAM:Bis = 29:1, 1% v/v HMPP). The Janus particles were immersed in the pregel solution for 12 hours so that the pregel could fill the voids of the particles. After irradiation with UV light for about 10 s, the pregel was polymerized, and pNIPAM inverse opal particles could be obtained with subsequent treatment of 5 M NaOH solution. The reflective spectra, optical images, and microstructures of the particles were also observed by the instruments mentioned above.

The NIR response behavior of the pNIPAM hydrogel particles
The prepared pNIPAM hydrogel particles were placed in a culture dish with fresh deionized water. The NIR light (808 nm; Xi Long Tech Co. Ltd.) was used to irradiate the hydrogel particles with a certain laser power. The color changes and spectra shifts of the particles were monitored by the instruments mentioned above.

Fabrication of inverse opal GelMA hydrogel particles
GelMA (0.15 g) was dissolved in 1 ml of deionized water with 10 μl of HMPP to obtain the pregel. The Janus particles were immersed in the pregel solution for 12 hours so that the pregel could fill the voids of the particles. After irradiation with UV light for about 10 s, the pregel was polymerized, and the inverse opal particles were obtained with subsequent treatment of 2 M HF solution. The reflective spectra, optical images, and microstructures of the particles were also observed by the instruments mentioned above. For cell culture, the GelMA hydrogel particles were sterilized by 75% ethyl alcohol immersion and UV light irradiation for 5 hours successively and washed by sterile HBSS before use.

Extraction of neonatal cardiomyocytes
Cardiomyocytes were extracted from 1- to 2-day neonatal Sprague-Dawley rat pups supplied by the Department of Comparative Medicine of Jinling Hospital (Nanjing, China). At first, the thoraxes of rat

pups were opened, and the hearts were surgically removed. After cleaning the connective tissue and blood clots, the hearts were cut into small pieces (about 0.5 to 1 mm^3). Next, the pieces were treated by HBSS with 0.02% (w/v) trypsin, 0.02% (w/v) pancreatin, and 0.05% (w/v) collagenase for 8 min at 37°C with continuous gentle shaking four times. Then, the digested cardiomyocytes and cardiac fibroblasts were collected into DMEM/F-12 medium (with 20% v/v FBS) solution and centrifuged by a centrifugal machine at 1000 rpm for 10 min. Subsequently, the cells were dispersed by DMEM/F-12 solution with 20% (v/v) FBS and 0.1 mM BrdU and cultured in a cell culture flask for 1.5 hours to separate cardiac fibroblasts from cardiomyocytes. Last, the suspended cardiomyocytes were separated and cultured on the GelMA hydrogel particles. All animal experiments were carried out in accordance with the Animal Ethics Committee of the Southeast University (no. 20180326003) and were conducted in compliance with the regulations for the Administration of Affairs Concerning Experimental Animals of China.

Cardiomyocytes culture and monitor

The cardiomyocytes were cultured with DMEM/F-12 medium containing 20% (v/v) FBS and 1% (v/v) penicillin-streptomycin, 0.1 mM BrdU in a humidified incubator with a constant temperature of 37°C, and 5% (v/v) CO_2 for the first 3 days of culture. Subsequently, the cardiomyocytes were continuously cultured and supplemented by the normal medium without BrdU. The particles with cardiomyocytes were immunostained on day 7 at room temperature. Samples were immersed in 4% (v/v) paraformaldehyde/PBS solution and 0.25% (v/v) Triton X-100/PBS solution for 0.5 hours successively to immobilize protein and permeabilize cytomembrane, respectively. Then, the samples were counterstained with Alexa Fluor 488 phalloidin (1:400 dilution) and DAPI (1:1000 dilution in PBS) for F-actin and nuclei staining. Between each step, the samples were gently washed with PBS at least three times. The fluorescence staining was observed by a CLSM (Zeiss LSM700 Zeiss, Heidenheim, Germany).

SUPPLEMENTARY MATERIALS

Supplementary material for this article is available at http://advances.sciencemag.org/cgi/content/full/6/2/eaay1438/DC1

The calculation of the size of the nanoparticles in the mix solution

Fig. S1. The change of charge (zeta potential) of the mixed solution and sedimentation time of the silica nanoparticles.

Fig. S2. Optical image and SEM image characterization of spherical particles and Janus SCPs.

Fig. S3. The microstructure of the junction of the two domains and the effect of GO concentration on the ratio of the major axis and minor axis.

Fig. S4. Relationships between the Janus SCP radius and the flow rate.

Fig. S5. Relationships of the Janus SCP radius with the concentration of mixed GO.

Fig. S6. Reflection microscope images of Janus SCPs.

Fig. S7. The relationships between the spectra and GO concentration or observed angles.

Fig. S8. The reflection microscope images and microstructure characterization of the orange Janus particles and the hybrid structure with pNIPAM.

Fig. S9. Reflection microscope image characterization of the red and green Janus SCPs, the hybrid structure with pNIPAM, and the corresponding inverse opal pNIPAM Janus SCPs.

Fig. S10. The optical microscope images of the structural color variation process of the hydrogel Janus SCPs during half photothermal response cycles.

Fig. S11. The photothermal responsive capability of the pNIPAM hydrogel Janus SCPs under NIR light.

Fig. S12. The results of the cardiomyocyte MTT assays.

Fig. S13. Reflection microscope images and spectra characterization of the Janus SCPs, the hybrid structure with GelMA, and the inverse opal GelMA Janus SCPs.

Fig. S14. The effect of various isoproterenol concentrations.

Table S1. Zeta potential characterization of silica nanoparticle solution, GO solution, and silica nanoparticles/GO solution, respectively.

Movie S1. The spherical SCPs in fluid.

Movie S2. The Janus SCPs in fluid.

Movie S3. The photothermal response process of a pNIPAM hydrogel Janus SCP.

Movie S4. The cardiomyocytes beating derived color change of a GelMA hydrogel SCP.

REFERENCES AND NOTES

1. J. Zi, X. Yu, Y. Li, X. Hu, C. Xu, X. Wang, X. Liu, R. Fu, Coloration strategies in peacock feathers. *Proc. Natl. Acad. Sci. U.S.A.* **100**, 12576–12578 (2003).
2. M. Kolle, P. M. Salgard-Cunha, M. R. J. Scherer, F. Huang, P. Vukusic, S. Mahajan, J. J. Baumberg, U. Steiner, Mimicking the colourful wing scale structure of the Papilio blumei butterfly. *Nat. Nanotechnol.* **5**, 511–515 (2010).
3. P. V. Braun, Materials Science: Colour without colourants. *Nature* **472**, 423–424 (2011).
4. G. Isapour, M. Lattuada, Bioinspired stimuli-responsive color-changing systems. *Adv. Mater.* **30**, 1707069 (2018).
5. Z. Chen, F. Fu, Y. Yu, Y. Shang, H. Wang, Y. Zhao, Cardiomyocytes actuated *Morpho* butterfly wings. *Adv. Mater.* **31**, 1805431 (2019).
6. D. Wang, V. Salgueiriño-Maceira, L. M. Liz-Marzán, F. Caruso, Gold-silica inverse opals by colloidal crystal templating. *Adv. Mater.* **14**, 908–912 (2002).
7. O. D. Velev, Self-assembly of unusual nanoparticle crystals. *Science* **312**, 376–377 (2006).
8. S. Kim, A. N. Mitropoulos, J. D. Spitzberg, H. Tao, D. L. Kaplan, F. G. Omenetto, Silk inverse opals. *Nat. Photonics* **6**, 818–823 (2012).
9. Y. Yue, T. Kurokawa, M. A. Haque, T. Nakajima, T. Nonoyama, X. Li, I. Kajiwara, J. P. Gong, Mechano-actuated ultrafast full-colour switching in layered photonic hydrogels. *Nat. Commun.* **5**, 4659 (2014).
10. M. Wang, L. He, W. Xu, X. Wang, Y. Yin, Magnetic assembly and field-tuning of ellipsoidal-nanoparticle-based colloidal photonic crystals. *Angew. Chem. Int. Ed.* **24**, 7077–7081 (2015).
11. D. Ge, E. Lee, L. Yang, Y. Cho, M. Li, D. S. Gianola, S. Yang, A robust smart window: Reversibly switching from high transparency to angle-independent structural color display. *Adv. Mater.* **27**, 2489–2495 (2015).
12. C. Liu, H. Ding, Z. Wu, B. Gao, F. Fu, L. Shang, Z. Gu, Y. Zhao, Tunable structural color surfaces with visually self-reporting wettability. *Adv. Funct. Mater.* **26**, 7937–7942 (2016).
13. F. Fu, Z. Chen, Z. Zhao, H. Wang, L. Shang, Z. Gu, Y. Zhao, Bio-inspired self-healing structural color hydrogel. *Proc. Natl. Acad. Sci. U.S.A.* **114**, 5900–5905 (2017).
14. C. Avci, I. Imaz, A. Carné-Sánchez, J. A. Pariente, N. Tasios, J. Pérez-Carvajal, M. I. Alonso, A. Blanco, M. Dijkstra, C. López, D. Maspoch, Self-assembly of polyhedral metal-organic framework particles into three-dimensional ordered superstructures. *Nat. Chem.* **10**, 78–84 (2018).
15. A. A. Jelle, K. K. Ghuman, P. G. O'Brien, A. Hmadeh, A. Sandhel, D. D. Perovic, C. V. Singh, C. A. Mims, G. A. Ozin, Highly efficient ambient temperature CO_2 photomethanation catalyzed by nanostructured RuO_2 on silicon photonic crystal support. *Adv. Energy Mater.* **8**, 1702277 (2018).
16. T. M. Choi, J.-G. Park, Y.-S. Kim, V. N. Manoharan, S.-H. Kim, Osmotic-pressure-mediated control of structural colors of photonic capsules. *Chem. Mater.* **27**, 1014–1020 (2015).
17. L. Shang, Y. Cheng, Y. Zhao, Emerging droplet microfluidics. *Chem. Rev.* **117**, 7964–8040 (2017).
18. H. Wang, H. Gu, Z. Chen, L. Shang, Z. Zhao, Z. Gu, Y. Zhao, Enzymatic inverse opal hydrogel particles for biocatalyst. *ACS Appl. Mater. Interfaces* **9**, 12914–12918 (2017).
19. H. Wang, Z. Zhao, Y. Liu, C. Shao, F. Bian, Y. Zhao, Biomimetic enzymes cascade reaction system in microfluidic electrospray microcapsules. *Sci. Adv.* **4**, eaat2816 (2018).
20. J. Ge, Y. Yin, Responsive photonic crystals. *Angew. Chem. Int. Ed.* **50**, 1492–1522 (2011).
21. H. Gu, Y. Zhao, Y. Cheng, Z. Xie, F. Rong, J. Li, B. Wang, D. Fu, Z. Gu, Tailoring colloidal photonic crystals with wide viewing angles. *Small* **9**, 2266–2271 (2013).
22. H. Wang, Q. Xu, L. Shang, J. Wang, F. Rong, Z. Gu, Y. Zhao, Boronate affinity molecularly imprinted inverse opal particles for multiple label-free bioassays. *Chem. Commun.* **52**, 3296–3299 (2016).
23. T. Y. Lee, T. M. Choi, T. S. Shim, R. A. M. Frijns, S. H. Kim, Microfluidic production of multiple emulsions and functional microcapsules. *Lab. Chip* **16**, 3415–3440 (2016).
24. K. R. Phillips, G. T. England, S. Sunny, E. Shirman, T. Shirman, N. Vogel, J. Aizenberg, A colloidoscope of colloid-based porous materials and their uses. *Chem. Soc. Rev.* **45**, 281–322 (2016).
25. J. Hou, M. Li, Y. Song, Recent advances in colloidal photonic crystal sensors: Materials, structures and analysis methods. *Nano Today* **22**, 132–144 (2018).
26. Y. Xu, H. Wang, C. Luan, F. Fu, B. Chen, H. Liu, Y. Zhao, Porous hydrogel encapsulated photonic barcodes for multiplex microRNA quantification. *Adv. Funct. Mater.* **28**, 1704458 (2018).
27. J. H. Lee, P. E. Loya, J. Lou, E. L. Thomas, Dynamic mechanical behavior of multilayer graphene via supersonic projectile penetration. *Science* **346**, 1092–1096 (2014).
28. J. Wang, L. Sun, M. Zou, W. Gao, C. Liu, L. Shang, Z. Gu, Y. Zhao, Bioinspired shape-memory graphene film with tunable wettability. *Sci. Adv.* **3**, e1700004 (2017).
29. H. Cheng, Y. Huang, G. Shi, L. Jiang, L. Qu, Graphene-based functional architectures: Sheets regulation and macrostructure construction toward actuators and power generators. *Acc. Chem. Res.* **50**, 1663–1671 (2017).

30. J. Wang, W. Gao, H. Zhang, M. Zou, Y. Chen, Y. Zhao, Programmable wettability on photo-controlled graphene film. *Sci. Adv.* **4**, eaat7392 (2018).

31. C. Luo, W. Lv, C. Qi, L. Zhong, Z. Pan, J. Li, F. Kang, Q. Yang, Realizing ultralow concentration gelation of graphene oxide with artificial interfaces. *Adv. Mater.* **31**, e1805075 (2019).

32. P. Bansal, A. P. Deshpande, M. G. Basavaraj, Hetero-aggregation of oppositely charged nanoparticles. *J. Colloid Interface Sci.* **492**, 92–100 (2017).

33. H. Wang, Y. Dong, M. Zhu, X. Li, A. A. Keller, T. Wang, F. Li, Heteroaggregation of engineered nanoparticles and kaolin clays in aqueous environments. *Water Res.* **80**, 130–138 (2015).

34. Y. Zhang, P. Han, H. Zhou, N. Wu, Y. Wei, X. Yao, J. Zhou, Y. Song, Highly brilliant noniridescent structural colors enabled by graphene nanosheets containing graphene quantum dots. *Adv. Funct. Mater.* **28**, 1802585 (2018).

35. H. Zhang, K. H. Fung, J. Hartmann, C. T. Chan, D. Wang, Controlled chainlike agglomeration of charged gold nanoparticles via a deliberate interaction balance. *J. Phys. Chem. C* **112**, 16830–16839 (2008).

36. C. P. Romero, R. I. Jeldres, G. R. Quezada, F. Concha, P. G. Toledo, Zeta potential and viscosity of colloidal silica suspensions: Effect of seawater salts, pH, flocculant, and shear rate. *Colloid Surface A* **538**, 210–218 (2018).

37. Y.-R. Shi, M.-P. Ye, L.-C. Du, Y.-X. Weng, Experimental determination of particle size-dependent surface charge density for silica nanospheres. *J. Phys. Chem. C* **122**, 23764–23771 (2018).

38. F. Peng, Y. Tu, D. A. Wilson, Micro/nanomotors towards in vivo application: Cell, tissue and biofluid. *Chem. Soc. Rev.* **46**, 5289–5310 (2017).

39. Y. Zhao, L. Shang, Y. Cheng, Z. Gu, Spherical colloidal photonic crystals. *Acc. Chem. Res.* **47**, 3632–3642 (2014).

40. Y. Yu, F. Fu, L. Shang, Y. Cheng, Z. Gu, Y. Zhao, Bio-inspired helical microfibers from microfluidics. *Adv. Mater.* **29**, 1605765 (2017).

41. Y. S. Zhang, J. Aleman, S. R. Shin, T. Kilic, D. Kim, S. A. M. Shaegh, S. Massa, R. Riahi, S. Chae, N. Hu, H. Avci, W. Zhang, A. Silvestri, A. S. Nezhad, A. Manbohi, F. De Ferrari, A. Polini, G. Calzone, N. Shaikh, P. Alerasool, E. Budina, J. Kang, N. Bhise, J. Ribas, A. Pourmand, A. Skardal, T. Shupe, C. E. Bishop, M. R. Dokmeci, A. Atala, A. Khademhosseini, Multisensor-integrated organs-on-chips platform for automated and continual in situ monitoring of organoid behaviors. *Proc. Natl. Acad. Sci. U.S.A.* **114**, E2293–E2302 (2017).

42. K. Zhu, N. Chen, X. Liu, X. Mu, W. Zhang, C. Wang, Y. S. Zhang, A general strategy for extrusion bioprinting of bio-macromolecular bioinks through alginate-templated dual-stage crosslinking. *Macromol. Biosci.* **18**, 1800127 (2018).

43. F. Fu, L. Shang, Z. Chen, Y. Yu, Y. Zhao, Bioinspired living structural color hydrogels. *Sci. Robot.* **3**, eaar8580 (2018).

44. J. U. Lind, T. A. Busbee, A. D. Valentine, F. S. Pasqualini, H. Yuan, M. Yadid, S. J. Park, A. Kotikian, A. P. Nesmith, P. H. Campbell, J. J. Vlassak, J. A. Lewis, K. K. Parker, Instrumented cardiac microphysiological devices via multimaterial three-dimensional printing. *Nat. Mater.* **16**, 303–308 (2017).

45. G. S. Ugolini, M. Rasponi, A. Pavesi, R. Santoro, R. Kamm, G. B. Fiore, M. Pesce, M. Soncini, On-chip assessment of human primary cardiac fibroblasts proliferative responses to uniaxial cyclic mechanical strain. *Biotechnol. Bioeng.* **113**, 859–869 (2016).

Citation: H. Wang, Y. Liu, Z. Chen, L. Sun, Y. Zhao, Anisotropic structural color particles from colloidal phase separation. *Sci. Adv.* **6**, eaay1438 (2020).

Science Advances

Anisotropic structural color particles from colloidal phase separation

Huan Wang, Yuxiao Liu, Zhuoyue Chen, Lingyu Sun and Yuanjin Zhao

ARTICLE TOOLS	http://advances.sciencemag.org/content/6/2/eaay1438
SUPPLEMENTARY MATERIALS	http://advances.sciencemag.org/content/suppl/2020/01/06/6.2.eaay1438.DC1
REFERENCES	This article cites 45 articles, 8 of which you can access for free http://advances.sciencemag.org/content/6/2/eaay1438#BIBL
PERMISSIONS	http://www.sciencemag.org/help/reprints-and-permissions

Use of this article is subject to the Terms of Service